J. P. Soaphys, Vol 5, N°1 (2025) C25A03
http://dx.doi.org/10.46411/jpsoaphys.2025.C25.03

Journal de physique de la SOAPHYS
http://www.soaphys.org/journal/
ISSN Print : *2630-0958*

Design and testing of a low-tech pedestal heliostat with its closed-loop tracking sensor for a micro concentrating solar power plant pilot in the Sahel: Case of CSP4Africa

Mahamadou MAIGA[1], Dimeba Osnoun Mubarak OUEDRAOGO[1], Aboubakar GOMNA[1], Kokouvi Edem N'TSOUKPOE[1*], Kokou Florent YIBOKOU[1], Hervé N. KENHAGHO[2]

[1] Laboratoire Énergies Renouvelables et Efficacité Énergétique (LabEREE), Département Génie Électrique, Énergétique et Industriel, Institut International d'Ingénierie de l'Eau et de l'Environnement (2iE), 01 BP 594 Ouagadougou 01, Burkina Faso
[2] Biomedical Laser and Optics Group, Department of Biomedical Engineering, University of Basel, Gewerbestrasse 14, Allschwil, 4123, Switzerland
** edem.ntsoukpoe@2ie-edu.org*

INFOS SUR L'A R T I C L E

Historique de l'article:
Reçu le : 04 Janvier 2024
Reçu en format revisé le : 29 Août 2024
Accepté le : 25 juin 2025

Keywords : Central receiver systems; Power tower plants; Pedestal heliostat; Closed-loop tracking; Four-quadrant LDR; CSP4Africa

Mots clés : Centrales solaires à tour ; Héliostat piédestal ; Suivi solaire en boucle fermée ; capteur LDR à quatre quadrants ; CSP4Africa

ABSTRACT

This study focuses on the design, construction, and test of a low-tech pedestal heliostat with its closed-loop tracking sensor for a micro CSP plant pilot. The design has involved the sizing of the 4 main components of the pedestal heliostat namely the support structure of the mirrors, the pedestal itself, the drive unit and the control unit. The 4 main components were then assembled to construct the heliostat pedestal that meets the aspirations of the CSP4Africa project. After the implementation of the heliostat, daily tests were carried out over several days to assess the ability of the device with its closed-loop tracking sensor to keep the focal spot on the target during the operating period of the CSP4Africa plant, which is from 9:00 am to 3:00 pm. Satisfactory results were met with a solar tracking error lower than 1° for a focal length of 5 m.

RESUME

Cette étude se concentre sur la conception, la construction et le test d'un héliostat piédestal de faible technicité pour un pilote de micro-centrale CSP. La conception a impliqué le dimensionnement des 4 composants principaux de l'héliostat piédestal, à savoir la structure de support des miroirs, le piédestal lui-même, l'organe d'entraînement et l'organe de commande. Les quatre composants principaux ont ensuite été assemblés pour construire l'héliostat piédestal qui répond aux aspirations du projet CSP4Africa. Après l'implémentation de l'héliostat, des tests de suivi solaire ont été réalisés pendant plusieurs jours pour évaluer la capacité de l'appareil avec son capteur de boucle fermée à garder la tâche focale à l'intérieur du cercle cible pendant la période de fonctionnement de la microcentrale CSP4Africa, qui va de 9h00 à 15h00. Des résultats satisfaisants ont été obtenus avec une erreur de suivi solaire inférieure à 1° pour une distance focale de 5 m.

I. INTRODUCTION

The Sahel, a semi-arid region situated to the south of the Sahara Desert in Africa, has been experiencing severe energy poverty for decades. This low energy accessibility is primarily attributed to the combination of the rapid growth of the population, the economic challenges, the isolation of the rural areas, the high dependence on fossil energies, and the limited access to affordable and sustainable energy [1,2]. Fortunately, the Sahelian region has abundant solar energy resources [3], offering a potential solution to its energy challenges through the implementation of appropriate systems, including concentrating solar-thermal power (CSP) [4,5].

CSP technologies could be a way of industrialization for the Sahel as compared to photovoltaic technology [6]. Indeed, the first worldwide CSP plant as well as the first worldwide thermodynamic solar pumps have been established in the Sahel [3] and major components of CSP plants can be designed locally using locally available materials and mankind. This could make it possible to influence the final production costs and increase the ability of the region to capitalize on the CSP technologies. Hence, various research activities on CSP technologies are underway in the region, particularly within the CSP4Africa project, which aims at developing a cost-effective small-scale CSP plant for decentralized microgrids by designing and experimenting their components using local low-cost materials [6]. For the power tower technology, two technologies of heliostat have been considered in the framework of the research and development activities within the project: the ganged heliostat [6,7] and the pedestal heliostat. The present study deals with the design, construction, and test of the low-tech and appropriate pedestal heliostat for small-scale concentrating solar power plants [8].

Heliostat is one of the main complex devices of a CSP plant based on power tower configuration [9]. Because of the apparent path of the sun relative to the

earth, the heliostat must constantly move to maintain its focal spot on the receiver of the plant. Two methods are used for this purpose (Figure 1): the open-loop tracking method (Figure 1a) and the closed-loop tracking method (Figure 1b) [10]. The open-loop tracking method is an approach based on the command and execution between the control unit and the drive unit of the heliostat, i.e., the control unit determines the position of the sun, deduces the ideal orientation of the heliostat, and sends the information to be executed by the drive unit. In the case of the closed-loop tracking method, the control unit goes well beyond sending the command to the drive unit. It checks by a feedback mechanism if the focal spot is actually on the receiver and possibly corrects the solar tracking error. The pedestal heliostat designed in the present article adopts a low-tech closed-loop tracking method to track the apparent path of the sun.

Several closed-loop tracking methods have been proposed for heliostats. In most cases, the feedback is taken from the focal spot by using sensors or cameras [9–13]. The sensors or cameras can be positioned on the heliostat [9,11], on the ground [10], in the way of the focal spot [12], or around the receiver [10,13] on the tower to detect and possibly correct solar tracking errors. In the present study, a four-quadrant light-dependent resistor (LDR) has been designed as a closed-loop tracking sensor for the subject pedestal heliostat. This sensor is placed on the way of the focal spot like Aiuchi et al. [12], but the latter used a two-quadrant LDR for an equatorial mount that is different from the adopted alt-azimuthal mount in CSP plants based on power tower configuration [14]. Four-quadrant LDR has been widely used to track the apparent path of the sun for solar panels and other applications [15–20]. To the best of the authors' knowledge, this is the first time to use it to concentrate sunlight for a heliostat for power tower plants by placing it in the way of the focal spot.

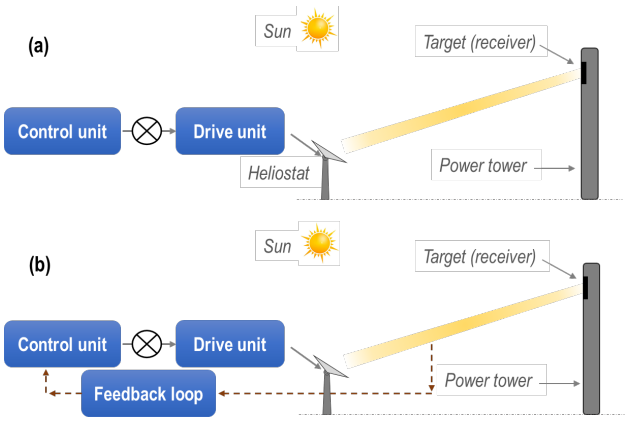

Figure 1: Illustration of the operating principle of a solar tracking method a) in an open-loop and b) in a closed-loop

II. HELIOSTAT DESIGN CONSIDERATIONS

A heliostat is a device designed to track the path of the sun in order to reflect its rays toward a small area, which is called receiver (Figure 2) [21]. The reflected rays of the heliostat are also referred to as the focal spot of the heliostat. Typically, there are 5 main technologies of heliostat in CSP plants based on power tower configuration [22]: pedestal heliostat, membrane heliostat (stressed, stretched, or bubble), ganged heliostat, carousel heliostat, and rotating heliostat field. The present study deals with the design of a pedestal heliostat. Because of their favorable cost per unity of size (area of the mirror installed on it) [22], pedestal heliostats are the most commonly used technology in large (≥ 50 MW_{el}) commercial CSP plants based on power tower configuration [23]. They are typically composed of four main components: (i) the support structure of the mirrors, (ii) the drive unit, (iii) the pedestal itself, and (iv) the control unit. Figure 2 shows the arrangement of the various components of a pedestal heliostat. The support structure of the mirrors has to be mobile according to the elevation and azimuthal paths of the sun. It is actioned by the drive unit under the command of the control unit. All these three components are supported by the pedestal in the presence of the wind load [24], which is relatively lower for small-size heliostats (from 1 m^2 to 48 m^2) [25].

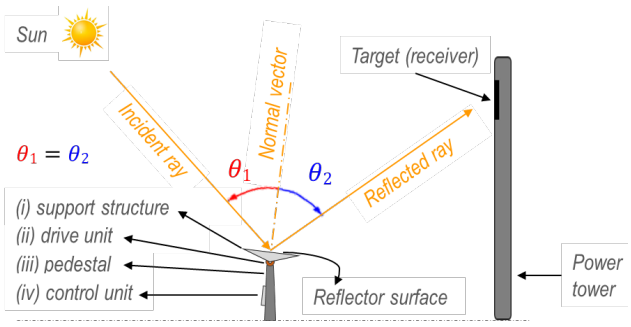

Figure 2: Illustration of the Snell-Descartes law applied to a heliostat constituted of its various components

The tracking accuracy of the heliostats can be affected by various optical error sources after the implementation. A distinction is made between the optical error sources [6,26,27] that reduce the thermal power of the reflected rays arriving at the receiver (dust, mirror deformation, cosine effect, shading effect, and blocking effect) and the optical error sources [9,22,26,28,29] that lead to the deviation of the reflected rays from the receiver (pedestal tilt, angular reference offset, mirror canting, non-orthogonality of the two-tracking axis, and incorrect location of the heliostat). The latter responsible for the deviation of the reflected rays is called solar tracking error source [22]. It can be avoided when designing the heliostat, unlike the first one, which reduces the thermal power of the reflected rays. The solar tracking error sources are mainly due to the exceeding of the yield strength of the material used to construct the heliostat, the mechanical backlash under the influence of the gravity load, the measuring instruments, the installation of the heliostat on unlevel ground, and the settling of the foundation due to the geotechnical properties of the soil and rainfall. All these aspects have been considered in the present design.

III. METHODOLOGY

The methodology of the present work is structured in 3 steps. The first step focuses on the design and sizing of the components of the pedestal heliostat. The sized components have then been constructed and assembled to form the pedestal heliostat that has been tested to validate the implemented tracking principle in the last step. The design, the sizing, and the construction procedures of each component are separately and deeply discussed in the next subsections. The sizing procedure is mainly based on the Eurocode 3 recommendations about the design of steel structures [30].

III.1. Design and sizing of the components

a - Support structure of the mirrors

The dimensions of the support structure depend on the dimensions of the mirror to be installed on it. The dimensions of the mirror also depend on the target dimensions of the receiver of the plant. The dimensions of the mirror should be less than the target dimensions of the receiver in order to avoid spillage losses. The receiver in this case is cavity type with a coil internal diameter of 0.7 m [6]. The target of the focal spot is the circular area of the receiver, which is 0.385 m^2. A square mirror with the technical specifications mentioned in Table 1 has been selected for the pedestal heliostat. The selection of this mirror is essentially based on local availability.

Table 1: Technical specifications of the selected mirror for the pedestal heliostat

Parameter	Unit	Value
Side	m	0.33
Thickness	m	0.003
Reflective area	m^2	0.109
Mass	kg	0.82

In order to reduce the cost of the drive unit by enlarging the reflective area of the pedestal heliostat, 16 square mirrors with the technical specifications mentioned before have been planned for the support structure (Figure 4a). These 16 mirrors have been incurved so that their focal spot forms a square of 0.33 m of side on the receiver of the plant [31]. The weight of the mirrors (W_m) is determined by Eq. (1). n is the number of mirrors to be installed on the support structure; m_m (kg) is the mass of one mirror; and g (m·s^{-2}) is the acceleration due to gravity.

$$W_m = n \cdot m_m \cdot g \quad (1)$$

The method presented by Peterka and Derisson [24], has been used to determine the wind load on the pedestal heliostat at 2 m of altitude. The speed of the wind at this altitude varies from 0 m·s^{-1} to 2 m·s^{-1} in Burkina Faso [32,33]. The wind speed of 3 m·s^{-1} has been considered as calculation assumption for the worst-case scenario. According to the method by Peterka and Derisson [24], the wind load is a function of 2 forces namely the drag force (F_x) and the lift one (F_z). They are determined by the Eqs. (2) and (3), respectively. Table 2 presents the drag and the lift coefficients resulting from the wind load for an isolated heliostat with the elevation angle of the support structure (α) and the wind direction (β) (Figure 3). The drag force is maximal when $\alpha = 90°$. The lift force is maximal when $\alpha = 30°$. Assumption is made to consider that $\beta = 0°$, as the wind direction is mostly on the north-south axis in the year in Ouagadougou [34] and also this is the worst-case scenario. C_{Fx} and C_{Fz} are the coefficients related to the drag force and the lift force of the wind, respectively; ρ (kg·m^{-3}) is the air density estimated to be 1.225 kg·m^{-3} for a temperature of 15 °C at atmospheric pressure; A_{ss} (m^2) the is total area of the support structure (Figure 4a).

$$F_X = C_{Fx} \cdot \frac{\rho}{2} \cdot V^2 \cdot A_{ss} \quad (2)$$

$$F_Z = C_{Fz} \cdot \frac{\rho}{2} \cdot V^2 \cdot A_{ss} \quad (3)$$

Table 2: Values of the coefficients resulting from the wind load [24]

	Fx, My Max	Fz, MHy Max	Mz Max	Stow Loads
	Peak loads			
α	90°	30°	90°	0°
β	0°	0°	65°	0°
Fx	4.0	2.1	3.7	0.6
Fz	1.0	2.8	0.5	0.9
MHy	0.25	0.6	0.15	0.2
Mz	0.29	0.06	0.7	0.02
	Mean loads			
α	90°	30°	90°	0°
β	0°	0°	65°	0°
Fx	2.0	1.0	1.6	0.1
Fz	0.3	1.35	0.3	0.1
MHy	0.02	0.25	0.02	0.02
Mz	0	0	0.25	0

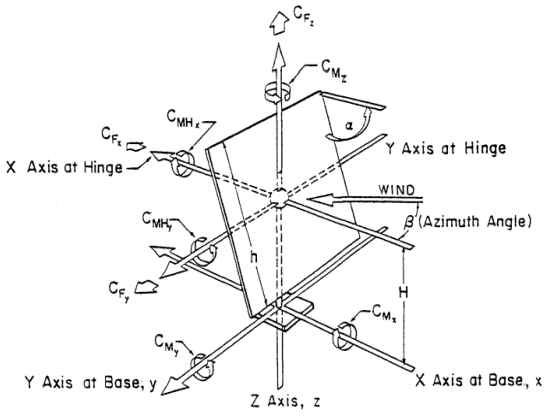

Figure 3: a) Illustration of the coefficients resulting from the wind load [24]

The last aspect to be considered is the selection of the square hollow steel tube that has been used to construct the support structure. This tube supports the load coming from the mirrors. The minimum moment of inertia required from it is derived from Eq. (4) by assimilating the support structure to a simply supported beam [30]. Dx (m)

is the deflection caused by the mirrors following the axis x (Figure 5); L (m) is the total length of the mirrors; W_{Dx} (N) is the load exerted by the mirrors under the influence of the wind according to the axis x; E (Pa) is the modulus of Young estimated to be 210 GPa; I_y (m^4) is the moment of inertia exerted linearly on the tube following the axis y.

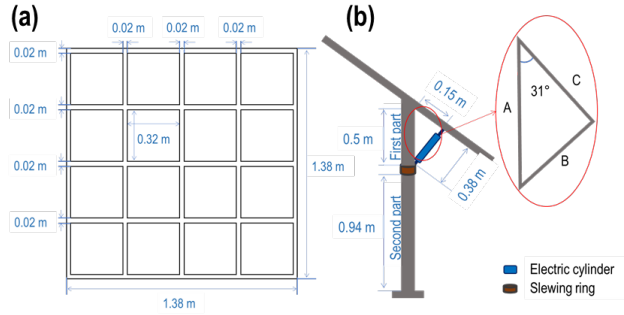

Figure 4: Presentation of a) the top view of the support structure of the mirrors and b) the front view of the pedestal heliostat with their dimensions

$$D_x \leq \frac{L}{200} \text{ where } D_x = \frac{5}{384} \cdot \frac{W_{D_x} L^4}{E I_y} \quad (4)$$

After the selection of the square hollow steel tube, Eq. (5) is verified to make sure that the support structure can resist the load coming from the mirrors under the influence of the wind. σ (Pa) is the bending stress caused by the mirrors under the influence of the wind load; σ_e (Pa) is the yield strength of the steel and is estimated to be 235 MPa; M_i (N·m) is the moment exerted by the mirrors under the influence of the wind according to the axis i; S_i (m^3) is the section modulus of the selected tube according to the axis i; W_{M_j}(N) is the load exerted by the mirrors under the influence of the wind according to the axis j.

$$\sigma = \frac{M_x}{S_x} + \frac{M_y}{S_y} \leq \sigma_e \text{ where } M_i = \frac{W_{M_j} \cdot L^2}{8} \quad (5)$$

Figure 5 illustrates the resulting forces from the mirrors on the support structure under the influence of the wind. Components of the load coming from the mirrors have been deducted in Eq. (6).

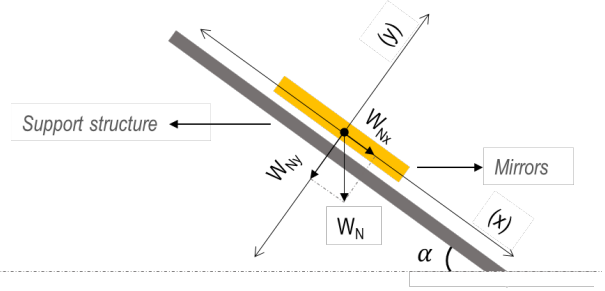

Figure 5: Illustration of the resulting forces from the mirrors on the support structure under the influence of the wind load

$$\begin{cases} W_{M_x} = W_M \cdot \sin\alpha \\ W_{M_y} = W_M \cdot \cos\alpha \end{cases} \quad \begin{cases} W_{D_x} = W_D \cdot \sin\alpha \\ W_{D_y} = W_D \cdot \cos\alpha \end{cases} \quad (6)$$

The load exerted by the mirrors on the support structure is maximal when $\alpha = 0°$ or $\alpha = 90°$. The case $\alpha = 90°$ has been considered because it corresponds to the worst-case scenario for the drag force of the wind load. By taking into account $\alpha = 90°$, Eq (6) becomes Eq. (7).

$$\begin{cases} W_{M_x} = W_M \\ W_{M_y} = 0 \end{cases} \quad \begin{cases} W_{D_x} = W_D \\ W_{D_y} = 0 \end{cases} \quad (7)$$

The ultimate limit state load (W_{ULS}) exerted by the mirrors on the support structure under the influence of the wind is considered for the moment by using Eq. (8). The reason is to guarantee the safety of the support structure [30].

$$W_{ULS} = W_M = \frac{1.35\,(W_m + Fx)}{L} \quad (8)$$

The service limit state load (W_{SLS}) exerted by the mirrors on the support structure under the influence of the wind is considered for the deflection by using Eq. (9). The reason is to guarantee a little bit flexibility for the support structure [30].

$$W_{SLS} = W_D = \frac{(W_m + Fx)}{L} \quad (9)$$

b - Drive unit

The drive unit is composed of the linear actuator and the slewing ring (Figure 4b). The linear actuator drives the support structure according to the elevation path of the sun while the slewing ring orients the support structure according to the azimuthal path of the sun. Each of these two actuators is crucial for the right operation of the heliostat. They are selected based on the minimum force and torque needed for the driving of the support structure under the influence of the wind load. Furthermore, they must be able to operate in a Sahelian weather, i.e., dusty and sunny environment. This corresponds to the IP65-rated equipment.

The minimum force needed for the driving of the support structure according to the elevation path of the sun (F_{la}) is determined by Eq. (10). W_{ss} (N) is the weight of the support structure; S is the factor of safety that has been fixed to 1.5.

$$F_{la} = (W_m + W_{ss} + F_z) \cdot S \quad (10)$$

The law of cosines (Eq. (11)) is used to determine the maximum and minimum length needed from the rod of the linear actuator according to the elevation path of the sun (Figure 4b). The yearly elevation path of the sun in Kamboinsin has been considered from 7:00 am to 5:00 pm in 2022 [35]. The maximum and minimum elevation of the sun are 88.87° on September 1st and 31.36° on April 23rd, respectively. α is the angle between the support structure and the pedestal of the heliostat.

$$B = \sqrt{A^2 + C^2 - 2 \cdot A \cdot C \cdot Cos(\alpha)} \quad (11)$$

The minimal torque needed for the driving of the support structure according to the azimuthal path of the sun (T_{sr}) determined by Eq. (12). W_{fpp} (N) is the weight of the first part of the pedestal; W_{la} (N) is the weight of the linear actuator.

$$T_{sr} = (W_m + W_{ss} + W_{fpp} + W_{la} + F_x) \cdot S \quad (12)$$

c - Pedestal

The pedestal is divided by the slewing ring into 2 parts as illustrated in Figure 4b. The first part supports the weight of the mirrors, the support structure and the linear actuator, while the second part supports the weight of all components of the heliostat, in addition to the first part of the pedestal. An assumption is made to consider that the pedestal is a continuous circular steel hollow tube. Its external diameter has been fixed to 60 mm and the appropriate internal diameter is determined by using Eq. (5). The moment of the force exerted on the pedestal is determined by Eq. (13). The worst-case scenario ($\alpha = 90°$) is considered again at the ultimate limit state load. x (m) is the moment arm estimated to be 0.5 m; W_{la} is the weight of the linear actuator.

$$M_y = 1.35 \cdot [(W_m + W_{ss} + W_{la}) \cdot g + F_x] \cdot x \quad (13)$$

After the selection of the circular hollow steel tube, the reduced slenderness of the pedestal ($\bar{\lambda}$) is determined by Eq. (14) to verify if the pedestal is likely to buckle face to the load coming from the mirrors, the support structure and the linear actuator under the influence of the wind [30]. λ is the geometric slenderness of the pedestal; l_{eff} is the effective length of the pedestal; and r is the radius of gyration of the pedestal.

$$\bar{\lambda} = \frac{\lambda}{93} \quad where \quad \lambda = \frac{l_{eff}}{r} \quad (14)$$

There is a risk of buckling of the pedestal if $\bar{\lambda} > 0.2$. When this is the case, the verification of Eq. (15) is necessary to clarify the situation. The dimensions of the selected tube have to be reviewed if the condition of tq. (15) is not verified. $\sigma_{applied}$ (Pa) is the applied axial stress on the pedestal; $\sigma_{critical}$ (Pa) is the critical stress to not be exceeded; $W_{supported}$ (N) is the axial load supported by the pedestal; χ represents the reduction factor for buckling based on the reduced slenderness. Its value is obtained from the buckling curves (a, b, c, and d) provided in the Eurocode 3 [30]; $\Phi(\bar{\lambda})$ is the imperfection factor derived from the buckling curves (a, b, c, and d) based on the cross-sectional class of the selected tube and the type of buckling; A (m^2) is the cross-sectional area of the selected tube; f_y (Pa) is the yield strength of the steel; and γ_{M1} is the partial safety factor for buckling resistance.

$$\sigma_{applied} \leq \sigma_{critical} \quad (15)$$

where:

$$\sigma_{applied} = \frac{W_{supported}}{A} = \frac{[(W_m + W_{ss} + W_{la}) \cdot g + F_x]}{A}$$

$$\sigma_{critical} = \chi \cdot \Phi(\bar{\lambda}) \cdot \frac{f_y}{\gamma_{M1}}$$

In the present study, $\Phi(\bar{\lambda}) = 1$, because the steel cross section in this case is classified as a plastic type.

d - Control unit

The configuration of the control unit is shown schematically in Figure 6. It pilots the support structure by commanding the actuators of the drive unit. It consists of five main electronic devices: (i) the Arduino board, (ii) the board of the actuators, (iii) the regulator, (iv) the data acquisition board, and (v) the closed-loop tracking sensor that is the four-quadrant LDR sensor. All these devices are locally available. A solar tracking principle compatible with the operation needed from the subject pedestal heliostat was first made. A four-quadrant LDR sensor has then been designed for this tracking principle. A solar tracking program in C language has eventually been proposed for the tracking principle on the Arduino software.

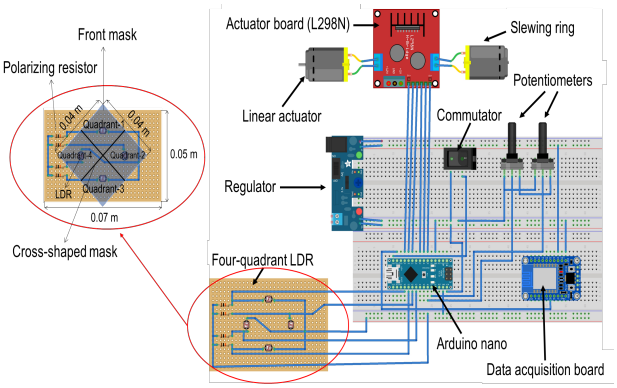

Figure 6: Configuration scheme of the control unit of the pedestal heliostat

The solar tracking principle adopted is based on a four-quadrant LDR sensor, which has been designed especially for the pedestal heliostat. The four-quadrant LDR sensor is placed on the way of the focal spot as illustrated in Figure 7. Its 4 LDRs face the focal spot and are covered by a front mask (Figure 6). The pedestal heliostat concentrates its focal spot on the receiver if the 4 LDRs of the sensor are shaded by the front mask (Figure 8a), otherwise, at least 1 of the 4 LDRs will deliver a signal because it is illuminated (Figure 8b). By comparing the signal delivered by the LDRs, the position of the heliostat can be readjusted by redirecting its focal spot toward the receiver (Figure 8c). This principle can be considered as a closed-loop solar tracking method because the control unit is commanding the drive unit by actively checking if the focal spot is really on the receiver. The LDRs in the odd-numbered quadrants (1 and 3) track the elevation path of the sun, while the LDRs in the even-numbered quadrants (2 and 4) track the azimuthal path of the sun. The

difference in delivered signals by the LDRs of the odd-numbered quadrants is referred to as LDRs1-3, while the difference in delivered signals by the LDRs of the even-numbered quadrants is referred to as LDRs2-4. The focal spot of the heliostat is focused on the target only if the 2 differences LDRs1-3 and LDRs2-4 are within the reference range [Lref, Href], that is also to say the 4 LDRs of the sensor are shaded by the front mask, as mentioned before.

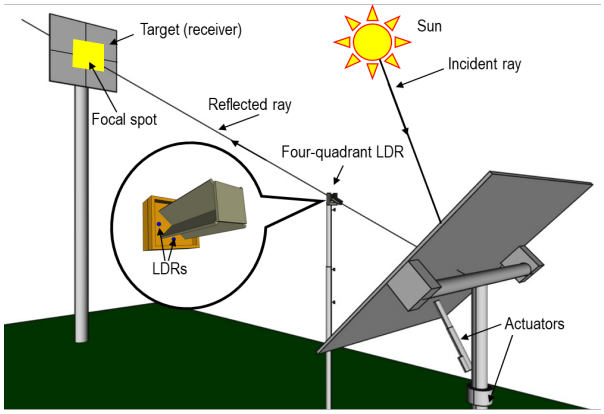

Figure 7: a) Illustration of the proposed solar tracking principle

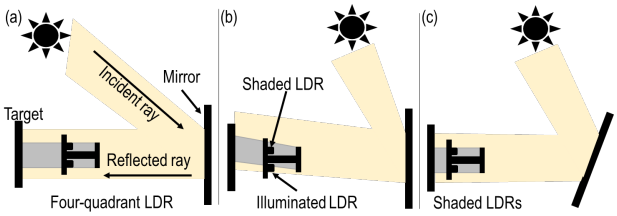

Figure 8: Illustration of the four-quadrant a) shaded by the front mask, b) partially illuminated by the focal spot, and c) re-shaded by the front mask after correction of the heliostat orientation

Four LDRs with technical specifications mentioned in Table 3 have been installed equidistantly at 2 cm from the center of the pre-printed circuit by forming a rhombus (Figure 6). A cross-shaped mask of 8 cm in length also separates the 4 LDRs from each other to define fairly their reception area which is called quadrant (Figure 6). Another front mask covers the 4 LDRs against the focal spot in order to know if the focal spot is well concentrated on the target (Figure 8a and b). The front mask is positioned atop the cross-shaped mask and has the same dimensions as the rhombus of 0.04 m in length formed by the cross-shaped mask (Figure 6). The LDRs are in the center of the quadrants and each is connected to a polarizing resistor in a voltage divider-bridge circuit.

Table 3: Technical specifications of the selected LDR for the sensor

Parameter	Unit	Value
Light resistance for 10 lux of illuminance	kΩ	30
Dark resistance	MΩ	3
γ response characteristic	(-)	0.7
Power dissipation	mW	100

The role of the polarizing resistors is to enable a stable conversion of the illumination received by the LDRs into a voltage range exploitable by the Arduino board. Furthermore, they limit the power dissipated by the LDRs. Teach of the 4 polarizing resistors to be selected for the sensor must satisfy the condition of the Eq. (16), which is deducted from the law of Joule. R (Ω) is the polarizing resistor; r (Ω) is the light resistance of the LDR for the maximum illuminance of the daytime (approximately 10^5 lux); P_{max} (W) is the maximum dissipation power of the LDR; and Vcc (V) is the supply voltage of the Arduino board, which is 5 V.

$$R \geq V_{cc} \cdot \sqrt{\left(\frac{r}{P_{max}}\right)} - r \qquad (16)$$

The resistor of the LDR is determined by Eq. (17) [20], which models the operation of the LDR.

$$r = R_0 \cdot \emptyset^{-\gamma} \qquad (17)$$

$\emptyset$ (lux) is the illuminance received by the LDR; γ is the response characteristic of the LDR; R_0 (Ω) is the nominal resistance of the LDR.

The flowchart presented in Figure 9 describes the proposed C program for the tracking principle. Two operation modes are available for the pedestal heliostat, the manual operation and the automatic one. At the beginning of the solar tracking, the user selects between the two modes of operation. The choice of the manual operation allows to adjust the orientation of the heliostat by using a joystick made up of 2 potentiometers and 1 commutator, while the automatic operation refers to an autonomous solar tracking of the pedestal heliostat in the absence of the clouds. The differences LDRs1-3 (for the linear actuator) and LDRs2-4 (for the slewing ring) must continuously be within the reference range [Lref, Href], as this means all the LDRs are shaded by the front mask because the focal spot points on the target. The actuators start-up, only if, at least one of the differences LDRs1-3 and LDRs2-4, is not within the reference range. This means that at least one of the 4 LDRs is illuminated, so the focal spot is no longer on the target.

III.2. Construction of the components

All components of the pedestal heliostat have been constructed locally with local labor. The selected hollow square steel tube was cut by an angle grinder. The tube pieces were then welded together to form the support structure of the mirrors. The drilling machine was used to make holes in the support structure for the screws that secure the mirrors to it. Washers were placed under the mirrors to enable them to be successfully incurved in a such way that the focal spots of the mirrors were superposed.

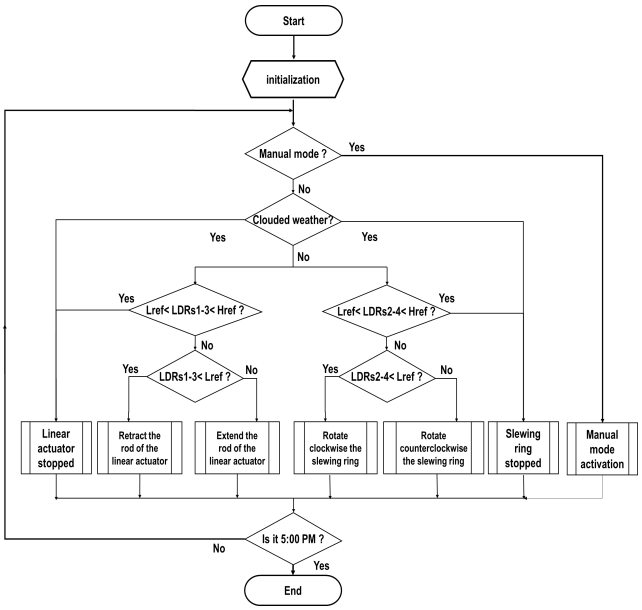

Figure 9: Flowchart of the solar tracking program

The circular steel tube selected for the pedestal was also cut using an angle grinder. The bracket of the linear actuator was welded to the first part of the pedestal, while the one of the slewing ring was welded to the second part of the pedestal. By the way, the linear actuator and the slewing ring were imported into the country with their control board after the sizing.

Concerning the closed-loop sensor, the LDRs were installed on the pre-printed circuit and fitted into a small 3D-printed container. The front and cross-shaped masks were all made from rigid cardboard. After the assembly of the components, the heliostat was installed on the CSP4Africa platform (12.464811°; -1.5519127°).

III.3. Test of the pedestal heliostat

After the preliminary checkout, solar tracking tests were carried out to assess the ability of the designed pedestal heliostat to maintain its focal spot on the target during the period of April to June 2023. Experimental protocols for installing the control unit of the pedestal heliostat, calibrating the 4-quadrant LDR sensor and solar tracking were set up. A one-meter-square wooden board graduated in decimeters was used as a target for the focal spot (Figure 10). The focal length of the spot is 5 m. The circle centered on the board represents the target area of the plant [6].

a - Protocol for installing the control unit

The following steps were taken to install the control unit of the pedestal heliostat.

- Step 1: Connect the actuators to their board
- Step 2: Connect the 4-quadrant LDR sensor, and the actuator board to the Arduino board
- Step 3: Attach the 4-quadrant LDR sensor to the tripod and place it in the way of the focal spot, i.e., between the pedestal heliostat and the target
- Step 4: Connect the regulator and the actuators board to the 12 V power supply

b - Protocol for calibrating the 4-quadrant LDR sensor

Before the test, it is important to make sure that the 4-quadrant LDR sensor is perfectly installed on the way of the focal spot. This process is called sensor calibration. It corrects the position of the sensor between the heliostat and the target, and is based on the four first steps below. Then, the solar tracking test begins.

- Step 1: Flip the switch to the ON position to activate to manual operation.
- Step 2: Use the potentiometers to guide the focal spot towards the center of the target.
- Step 3: Orient rigorously the closed-loop sensor in a such way that all 4 LDRs are shaded.
- Step 4: Flip the switch to the OFF position to activate the automatic operation.
- Step 5: Take a picture of the focal spot on the target every 10 minutes

c - Assessment of the solar tracking error

The solar tracking error is the difference between the actual and ideal orientation of the heliostat [10,28]. It also corresponds to the distance between the target and the centroid of the focal spot when the heliostat is operating. However, in the present study, it corresponds to the difference between the actual orientation of the heliostat at the beginning and the end of the solar tracking, as illustrated in Figure 10. It is estimated by the Eq. (18). Δx (m) is the horizontal variation of the centroid of the focal spot on the axis x; Δy (m) is the vertical variation of the centroid of the focal spot on the axis y; L_{focal} (m) is the focal length of the heliostat at the beginning of the test.

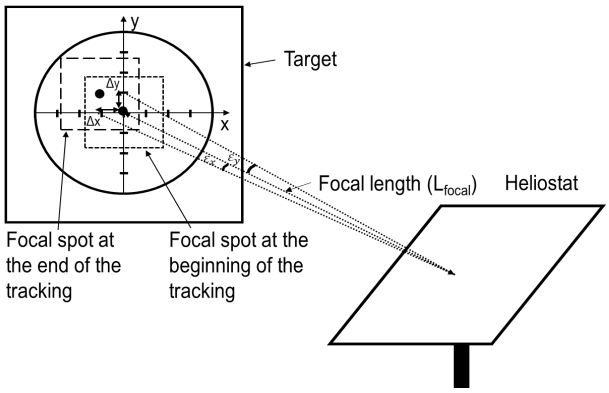

Figure 10: Illustration of the method adopted to assess the solar tracking error

$$\varepsilon = Arctan\left(\frac{\sqrt{\Delta x^2 + \Delta y^2}}{L_{focal}}\right) \quad (18)$$

IV. RESULTS AND DISCUSSION

IV.1. Sizing of the components

Table 4 presents the results of the sizing of the components of the designed pedestal heliostat. The moment of inertia of the appropriate square hollow steel tube should be greater than 0.44 cm^4 to avoid the deformation of the support structure face to the load coming from mirrors under the wind influence. The tube with a moment of inertia of 0.583 cm^4 has been selected in the catalog. This is the one with the moment of inertia right greater than 0.44 cm^4 in the catalog. Its technical specifications are presented in

Table 5.

The bending stress caused by the mirrors on the support structure with the selected tube is 70 MPa. This is approximately 3 times lower than the yield strength of the steel, which is 235 MPa, i.e., the support structure is more resistant with the selected tube face to the load coming from mirrors under the wind influence.

Table 4: Results of the sizing of the components of the pedestal heliostat

Concerned component	Parameter	Unit	Value
Support structure of the mirrors	Load of the mirrors	N	131.2
	Drag force of the wind	N	44.5
	Lift force of the wind	N	31.1
	ULS load of the mirrors	$N{\cdot}m^{-1}$	167
	SLS load of the mirrors	$N{\cdot}m^{-1}$	124
	Tube moment of inertia	cm^4	0.44
	Bending moment	N·m	44.3
	Bending stress	MPa	70
Drive unit	Minimum force needed from the linear actuator	N	423.5
	Minimum length needed from linear actuator	mm	374
	Maximum length needed from linear actuator	mm	522
	Minimum torque needed from the slewing ring	N·m	764
Pedestal	ULS bending moment	N·m	401
	Maximum internal diameter	mm	59
	Geometric slenderness	(-)	77
	Reduced slenderness	(-)	0.8
	Applied axial stress	MPa	2
	Critical stress	MPa	94
Control unit	Nominal resistance of the LDR	Ω	150 356
	Light resistance of the LDR for 10^5 lux (Maximum illuminance of daytime)	Ω	48
	Minimum resistance for the polarizing resistor	Ω	62

Table 5 : Technical specifications of the selected square hollow steel tube

Parameter	Unit	Value
Moment of inertia	cm^4	0.583
Thickness	cm	1.5
Side	cm	2
Modulus of the section	cm^3	0.637

The minimum force needed for the driving of the support structure according to the elevation path of the sun is 423.5 N. A linear actuator with 2400 N of force has been selected for the pedestal heliostat. More specifications are presented in Table 6.

Table 6: Technical specifications of the selected linear actuator

Parameter	Unit	Value
Force	N	2400
Maximum speed	$mm{\cdot}s^{-1}$	33
Length of the rod	mm	570
Supply voltage	Vdc	24
Protection class	-	IP65

The minimum torque needed for the driving of the support structure according to the azimuthal path of the sun is 764 N·m. A slewing ring with 805 N·m of torque has been selected for the pedestal heliostat. More specifications are presented in Table 7.

Table 7: Technical specifications of the selected slewing ring

Parameter	Unit	Value
Torque	N·m	805
Maximum speed	rpm	0.049
Supply voltage	Vdc	24
Protection class	-	IP55

The ULS bending moment on the pedestal is 401 N·m. Its external diameter has been fixed to 60.3 mm, and 59 mm deduced from the ULS bending moment as its maximum internal diameter to avoid buckling under the load supported. A circular steel tube with an internal diameter of 57.4 mm and an external diameter of 60.3 mm has been selected as a pedestal for the heliostat. More specifications are presented in Table 8. The applied axial stress on the selected tube is 2 MPa, while the critical stress to not be exceeded is 94 MPa. It is clear that the selected tube is able to resist the load coming from all components under the wind influence.

Table 8: Technical specifications of the circular tube selected as pedestal

Parameter	Unit	Value
Moment of inertia	cm^4	0.116
Internal diameter	mm	57.4
External diameter	mm	60.3
Radius of gyration	mm	208.13
Cross-sectional area	cm^2	2.7

The minimum value for the polarizing resistor of the four-quadrant LDR sensor is 62 Ω. Four similar

resistors of 220 Ω have been firstly selected for the sensor to convert the illimitation received by the LDRs into a voltage range exploitable by the Arduino board. The preliminary checkout will tell more about its ability to meet the need of polarizing.

IV.2. Assembly of the components

Figure 11 presents the process of the assembly of the components of the pedestal heliostat. After the construction of the support structure, the holes for the mirrors were made on it. It has then been connected to the first part of the pedestal through a bearing. The first part of the pedestal with the support structure already connected, has also been connected to the second part of the pedestal through the slewing ring. The linear actuator was simply screwed to its bracket between the support structure and the first part of the pedestal.

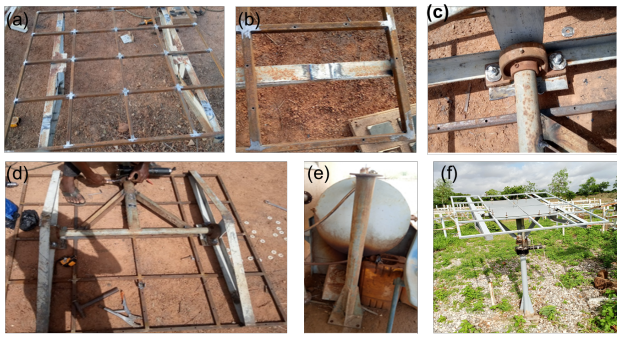

Figure 11: a) Support structure of the mirrors; b) Zoom on the holes of the screws securing the mirrors; c) Connection of the support structure to the first part of the pedestal using a bearing; d) Support structure connected to the first part of the pedestal; e) Second part of the pedestal; f) The installed pedestal heliostat

All constructed components of the pedestal heliostat, except for the control unit, have been painted light gray. The designed pedestal heliostat has then been installed on the CSP4Africa platform, as presented in Figure 11f. The control unit with its four-quadrant LDR sensor is separately presented in Figure 12.

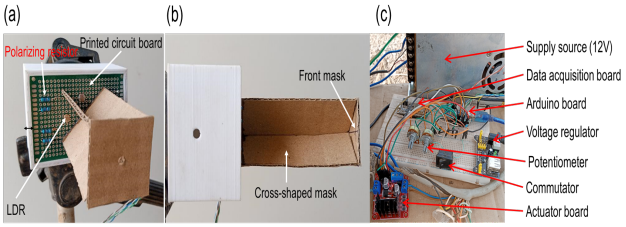

Figure 12: a) Control unit of the heliostat with its closed-loop tracking sensor in b) perspective, and c) face view

IV.3. Test of the designed pedestal heliostat

a - Preliminary checkout

Preliminary checkout was done to verify that all components of the designed pedestal heliostat satisfy the requirements needed. The linear actuator and the slewing ring were operated manually to confirm the proper alignment and orientation of the support structure of the heliostat, respectively. The linear actuator was able to align the support structure of the heliostat between the range of 0° to 90° (Figure 13a), as planned for the elevation movement of the heliostat. The slewing ring was also able to orient the support structure of the heliostat between the range of 0° to 180° (Figure 13b), as planned for the azimuth movement of the heliostat. These confirmations were necessary. They imply that the designed pedestal heliostat is able to operate during the daily availability of the solar resources in Kamboinsin, i.e., from the sunrise to sunset.

The flatness test of the support structure of the mirrors was also done to make sure that its above surface is rectilinear. This was the case, confirming that the mirrors can be easily mounted and canted over the pedestal heliostat to form the square focal spot of 0.33 m of side using the on-sun canting method [31].

Figure 13:a) Alignment of the support structure of the heliostat between the range of 0° to 90° and b) orientation of the support structure of the heliostat between the range of 0° to 180°

After installation, the pedestal tilt was also checked as it is a prevalent error source in heliostat fields of power tower plant. The measured angle of the pedestal with the inclinometer was 90±1°. This suggests that the pedestal was approximately parallel to the vertical of the location at the implementation of the heliostat. However, it should be noted that the pedestal tilt may appear over time, even if the solar tracking principle adopted by the designed pedestal heliostat is able to correct the deviation it can cause.

The control unit was tested by using the joystick consisting of 2 potentiometers and 1 commutator. In the automatic operation, the heliostat tracks autonomously the sun by focusing the sunlight onto the target. In the manual operation, the 2 potentiometers were also able to align and orient the support structure of the heliostat. Furthermore, the commutator could switch from the manual to automatic operation of the heliostat, and vice versa.

It should be mentioned that 3 sensors of four-quadrant LDR with various values (220 Ω, 1 kΩ, and 4.7 kΩ) of the polarizing resistor were designed as a closed-loop sensor. All three sensors were tested with the heliostat. The sensor with the polarizing resistor value of 4.7 kΩ was the only one to provide satisfactory results, i.e.,

to keep the focal spot of the heliostat inside the target circle of the one-meter-square wooden board, which represents the target area of the CSP4Africa plant. The focal spot was getting out of the target circle with the other 2 sensors during the operation of the heliostat. It was in fact oscillating around the target circle. It has even left the one-meter-square wooden board with a polarizing resistor value of 220 Ω. This may be explained by the sensitivity of the 4-quadrant LDR according to the luminosity. It is in fact a function of the value of the polarizing resistor. The lower the value of the polarizing resistor, the more sensitive the 4-quadrant LDR sensor is to the luminosity. The polarizing resistor value of 4.7 kΩ has eventually been selected for the closed-loop sensor of the heliostat.

b - Daily solar tracking test

The main goal of the daily solar tracking tests was to assess the ability of the pedestal heliostat with its closed-loop sensor to keep the focal spot inside the target circle during the operating period of the CSP4Africa plant, which is from 9:00 am to 3:00 pm. The tests were carried out over several days (May 16th, 17th, 23rd and 24th, 2023), with satisfactory results. During these daily tests, the control unit was able to keep the focal spot of the heliostat approximately inside the target circle. The image sequence of May 24th, 2023 in Figure 14 may bear witness to this. The image sequences for the other days are not presented in this paper. It should be pointed out that clouds often disrupt the operation of the control unit of the heliostat due to the significant drop in focal spot intensity. The heliostat was therefore paused by a fifth LDR when the sky was completely clouded.

Figure 14: Sequence of images of the focal spot during the solar tracking test done on May 24th, 2023

c - Assessment of the solar tracking error

During the daily solar tracking tests, the mirror spots were observed to disperse slightly and continuously while the mirrors remained perfectly canted. The edges of some mirror spots were even clearly visible at the end of the solar tracking test (Figure 15b), whereas all of the mirror spots were rigorously superposed at the beginning of the solar tracking (Figure 15a).

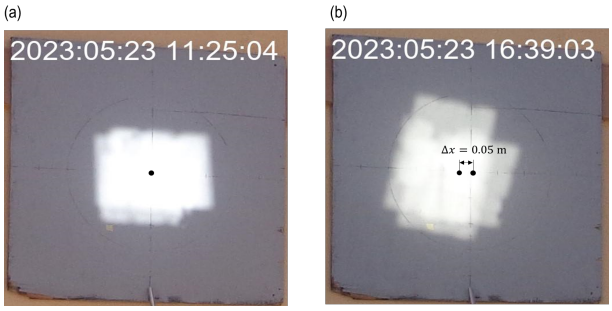

Figure 15: Focal spot of the heliostat at the a) beginning and b) end of solar tracking test carried out on May 17th, 2023

The assumption is made that the mirrors have remained canted during the solar tracking test and were also screwed to the support structure of the heliostat. However, they had different angles due to the canting. The dispersion of the spots throughout the day can be explained by the apparent path of the sun, as the next day the spots were approximately found superposed again at the beginning of a new solar tracking test. A simulation with 3 mirrors was performed on the GeoGebra software to corroborate the observation made. In Figure 16, (Dn) represents the reflected ray of the mirror n during the solar tracking test. It can be observed that all the (Dn)s converge toward point C (center of the target circle) when the sun is rising in the east (Figure 16a). By contrast, the (Dn)s no longer converge toward point C when the sun (S) is setting in the west (Figure 16b). This fact is evidenced by the dispersion of mirror spots on the target, thereby increasing the size of the focal spot and the solar tracking error of the pedestal heliostat.

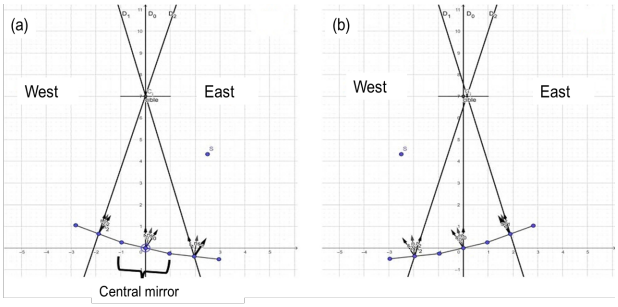

Figure 16: Simulation of the spot dispersion on the GeoGebra software a) at the beginning and b) at the end of the solar tracking test.

The variation of the centroid of the focal spot following the horizontal and vertical axes of the target was estimated to be 0.05 m and 0.0 m at the end of the solar tracking test done on May 17th, 2023, respectively. The numerical application of Eq. (18) allows to assess the solar tracking error to $\varepsilon = 0.57°$ for the solar tracking test done on May 17th, 2023 (Table 9). The solar tracking errors for the other days are presented in Table 9.

Table 9: Solar tracking errors of the daily solar tracking carried out on May, 16th, 17th, 23rd and 24th, 2023

Day of the test	Solar tracking error

May 16th, 2023	0.49°
May 17th, 2023	0.57°
May 23rd, 2023	0.92°
May 24th, 2023	0.74°

The solar tracking errors vary depending on the test days. This variation can be attributed to the calibration accuracy of the closed-loop sensor, as well as the daily and seasonal paths of the sun that continuously change in the year. The same calibration accuracy of the closed-loop sensor could not be achieved each time, as the control unit was disassembled at the end of each tracking session and reassembled just before the beginning of the next solar tracking test. The highest calibration accuracy of the closed-loop sensor was achieved during the solar tracking test done on May 16th, 2023.

V. CONCLUSION

The energy poverty in the Sahel, more openly sub-saharan Africa, can be addressed through innovative and locally adapted solutions. CSP technologies could be counted among these solutions by prioritizing simplicity, durability, and local integration. The CSP4Africa project is a glimpse into how this is possible. A pedestal heliostat with its closed-loop solar tracking sensor has been designed, constructed, and tested using only available materials and mankind in the Sahel.

The design has involved the sizing of the 4 main components of the pedestal heliostat, namely the support structure of the mirrors, the pedestal itself, the drive unit composed of a linear actuator and a slewing ring, and the control unit made up of an Arduino board, an actuator board, a regulator, a data acquisition board, and a closed-loop tracking sensor which is the designed four-quadrant LDR. The 4 main components were then assembled to construct the pedestal heliostat that meets the aspirations of the CSP4Africa project. After the implementation of the designed pedestal heliostat, daily tests were carried out over several days to assess the ability of the device with its closed-loop tracking sensor to keep the focal spot inside the target circle during the operating period of the CSP4Africa plant, which is from 9:00 am to 3:00 pm. Satisfactory results were met with a solar tracking error lower than 1° for a focal length of 5 m. Full-year tests are still required to validate the proposed solar tracking principle and conclude about the potentiality of the designed pedestal heliostat to solve the energy challenges in the Sahel, more openly sub-Saharan Africa.

ACKNOWLEDGEMENTS

This work has been supported by the European Commission within the framework of H2020/LEAP-RE [grant number 963530].

Mahamadou MAIGA is kindly grateful to the German Academic Exchange Service (DAAD) for funding his PhD studies [grant number 57587957, 2021].

REFERENCES

[1] Nalule VR. Energy Poverty and Access Challenges in Sub-Saharan Africa: The role of regionalism. Springer; 2018.

[2] González-Eguino M. Energy poverty: An overview. Renewable and Sustainable Energy Reviews 2015;47:377–85. https://doi.org/10.1016/j.rser.2015.03.013.

[3] N'tsoukpoe KE, Lekombo SC, Kemausuor F, Ko GK, Diaw EHB. Overview of solar thermal technology development and applications in West Africa: Focus on hot water and its applications. Scientific African 2023;21:e01752. https://doi.org/10.1016/j.sciaf.2023.e01752.

[4] Azoumah Y, Ramdé EW, Tapsoba G, Thiam S. Siting guidelines for concentrating solar power plants in the Sahel: Case study of Burkina Faso. Solar Energy 2010;84:1545–53. https://doi.org/10.1016/j.solener.2010.05.019.

[5] Barlev D, Vidu R, Stroeve P. Innovation in concentrated solar power. Solar Energy Materials and Solar Cells 2011;95:2703–25. https://doi.org/10.1016/j.solmat.2011.05.020.

[6] N'Tsoukpoe KE, Azoumah KY, Ramde E, Fiagbe AKY, Neveu P, Py X, et al. Integrated design and construction of a micro-central tower power plant. Energy for Sustainable Development 2016;31:1–13. https://doi.org/10.1016/j.esd.2015.11.004.

[7] SESHIE YM. Modélisation et expérimentation d'une microcentrale solaire a concentration. http://documentation.2ie-edu.org/cdi2ie/opac_css/index.php?lvl=author_see&id=17880. Documentation Institut 2iE; 2018.

[8] Seshie YM, N'Tsoukpoe KE, Neveu P, Coulibaly Y, Azoumah YK. Small scale concentrating solar plants for rural electrification. Renewable and Sustainable Energy Reviews 2018;90:195–209. https://doi.org/10.1016/j.rser.2018.03.036.

[9] Zhu G, Augustine C, Mitchell R, Muller M, Kurup P, Zolan A, et al. Roadmap to Advance Heliostat Technologies for Concentrating Solar-Thermal Power. National Renewable Energy Lab. (NREL), Golden, CO (United States); 2022. https://doi.org/10.2172/1888029.

[10] Sattler JC, Röger M, Schwarzbözl P, Buck R, Macke A, Raeder C, et al. Review of heliostat calibration and tracking control methods. Sol Energy 2020;207:110–32. https://doi.org/10.1016/j.solener.2020.06.030.

[11] Mahboob K, Awais Q, Khan A, Fawad T, Rasool M, Nawaz Q, et al. Selection of Sensors for Heliostat of

Concentrated Solar Thermal Tower Power Plant. Engineering Proceedings 2021;12:41.
[12] Aiuchi K, Yoshida K, Onozaki M, Katayama Y, Nakamura M, Nakamura K. Sensor-controlled heliostat with an equatorial mount. Solar Energy 2006;80:1089–97. https://doi.org/10.1016/j.solener.2005.10.007.
[13] Convery MR. Closed-loop control for power tower heliostats. High and Low Concentrator Systems for Solar Electric Applications VI, vol. 8108, SPIE; 2011, p. 142–9. https://doi.org/10.1117/12.898564.
[14] Behar O, Khellaf A, Mohammedi K. A review of studies on central receiver solar thermal power plants. Renewable and Sustainable Energy Reviews 2013;23:12–39. https://doi.org/10.1016/j.rser.2013.02.017.
[15] Jaanaki SM, Mandal D, Hullikeri HH, V S, A AS. Performance Enhancement of Solar Panel Using Dual Axis Solar Tracker. 2021 International Conference on Design Innovations for 3Cs Compute Communicate Control (ICDI3C), 2021, p. 98–102. https://doi.org/10.1109/ICDI3C53598.2021.00028.
[16] Hammoumi AE, Motahhir S, Ghzizal AE, Chalh A, Derouich A. A simple and low-cost active dual-axis solar tracker. Energy Science & Engineering 2018;6:607–20. https://doi.org/10.1002/ese3.236.
[17] Wang J-M, Lu C-L. Design and implementation of a sun tracker with a dual-axis single motor for an optical sensor-based photovoltaic system. Sensors 2013;13:3157–68.
[18] LINGALA VENKATESWARLU C, SESHAIAH T. Dual sun tracking system by using four quadrant sensor n.d.
[19] Lee C-Y, Chou P-C, Chiang C-M, Lin C-F. Sun tracking systems: a review. Sensors 2009;9:3875–90.
[20] Marinho F, Carvalho CM, Apolinário FR, Paulucci L. Measuring light with light-dependent resistors: an easy approach for optics experiments. Eur J Phys 2019;40:035801. https://doi.org/10.1088/1361-6404/ab11f1.
[21] Kallos G. Vulnerability of Energy to Climate. In: Pielke RA, editor. Climate Vulnerability, Oxford: Academic Press; 2013. https://doi.org/10.1016/B978-0-12-384703-4.00301-4.
[22] Maiga M, N'Tsoukpoe KE, Gomna A, Fiagbe YAK. Sources of solar tracking errors and correction strategies for heliostats. Renewable and Sustainable Energy Reviews 2024;203:114770. https://doi.org/10.1016/j.rser.2024.114770.
[23] NREL. Operational | Concentrating Solar Power Projects | NREL n.d. https://solarpaces.nrel.gov/by-status/operational (accessed April 30, 2022).
[24] Peterka JA, Derickson RG. Wind load design methods for ground-based heliostats and parabolic dish collectors. Sandia National Lab. (SNL-NM), Albuquerque, NM (United States); 1992. https://doi.org/10.2172/7105290.
[25] Yerudkar AN, Kumar D, Dalvi VH, Panse SV, Gaval VR, Joshi JB. Economically feasible solutions in concentrating solar power technology specifically for heliostats – A review. Renewable and Sustainable Energy Reviews 2024;189:113825. https://doi.org/10.1016/j.rser.2023.113825.
[26] El Ydrissi M, Ghennioui H, Bennouna EG, Farid A. A review of optical errors and available applications of deflectometry technique in solar thermal power applications. Renewable and Sustainable Energy Reviews 2019;116:109438. https://doi.org/10.1016/j.rser.2019.109438.
[27] Hachicha AA, Al-Sawafta I, Ben Hamadou D. Numerical and experimental investigations of dust effect on CSP performance under United Arab Emirates weather conditions. Renewable Energy 2019;143:263–76. https://doi.org/10.1016/j.renene.2019.04.144.
[28] Escobar-Toledo M, Arancibia-Bulnes CA, Iriarte-Cornejo C, Waissman J, Riveros-Rosas D, Cabanillas RE, et al. Heliostat image drift behavior for different error sources. J Renewable Sustainable Energy 2014;6. https://doi.org/10.1063/1.4872465.
[29] Martínez-Hernández A, Gonzalo IB, Romero M, González-Aguilar J. Drift analysis in tilt-roll heliostats. Sol Energy 2020;211:1170–83. https://doi.org/10.1016/j.solener.2020.10.057.
[30] Morel J. Calcul des structures métalliques selon l'eurocode 3. https://trid.trb.org/view/1004578. 1994.
[31] Ren L, Wei X, Lu Z, Yu W, Xu W, Shen Z. A review of available methods for the alignment of mirror facets of solar concentrator in solar thermal power system. Renewable and Sustainable Energy Reviews 2014;32:76–83. https://doi.org/10.1016/j.rser.2013.12.006.
[32] Zoma V, Tarama WJI, Ouédraogo J. Variabilité climatique dans la commune rurale de Seytenga au Burkina Faso. Les Cahiers de l'ACAREF 2022;4:320–34. https://hal.science/hal-03645488/.
[33] Direction de la météorologie du Burkina Faso. Bulletin météorologique décadaire. Burkina Faso: http://wamis.gmu.edu/countries/burkina/bad06072.pdf; 2016.
[34] Simulation de données climatiques et météorologiques historiques pour Ouagadougou. meteoblue weather 2023. https://www.meteoblue.com/fr/meteo/historyclimate/climatemodelled/ouagadougou_burkina-faso_2357048 (accessed October 26, 2023).
[35] SunEarthtools n.d. https://www.sunearthtools.com/dp/tools/pos_sun.php?lang=fr (accessed October 1, 2023).